Assembly of the IXPE mirror modules

Stephen D. Bongiorno[a], Jeffery J. Kolodziejczak[a], Kiranmayee Kilaru[b], Ron Eng[a], Mark Stahl[a], Wayne H. Baumgartner[a], Nicholas Thomas[a], Jagan Ranganathan[a], Brian D. Ramsey[a], and John Tucker[c]

[a]NASA Marshall Space Flight Ctr., Huntsville AL 35812, USA
[b]USRA, Marshall Space Flight Ctr., Huntsville AL 35812, USA
[c]ESCCA, Marshall Space Flight Ctr., Huntsville AL 35812, USA

ABSTRACT

Expected to launch in December 2021, the Imaging X-ray Polarimetry Explorer (*IXPE*) is a NASA Astrophysics Small Explorer Mission with significant contributions from the Italian space agency (ASI). Three identical x-ray telescopes combine to form the *IXPE* Observatory. Each is comprised of a 4-m-focal length mirror module assembly (MMA, provided by Marshall Space Flight Center) that focuses x-rays onto a polarization-sensitive, imaging detector (contributed by ASI-funded institutions). This paper describes the now-completed assembly process for the 3 flight and one spare mirror modules, and compares as-tested calibrated performance with as-built metrology data. Unexpected challenges and lessons-learned are also discussed.

Keywords: x-ray optics, IXPE, electroformed nickel, x-ray

1. INTRODUCTION

The Imaging X-ray Polarimetry Explorer (*IXPE*)[1–4] is a NASA Small Explorer mission that will perform the first imaging x-ray polarimetry observations of astrophysical targets, essentially opening a new field of study. *IXPE* will observe a wide range of sources over the 2-8 keV energy band, including active galactic nuclei, microquasars, pulsars, pulsar wind nebulae, magnetars, accreting x-ray binaries, supernova remnants, and the Galactic center. Scientific topics that will be investigated through the study of polarized x-ray emission include the geometries of mass flows, x-ray emission regions, and magnetic fields; the physical processes that lead to particle acceleration and x-ray emission; and the physical effects of gravitational, electric, and magnetic fields at their extreme limits.[5]

This proceedings paper will describe the assembly process of the *IXPE* Mirror Module Assemblies from a post-build perspective. The as-built mechanical design will be described in §2, the mirror shell alignment process described in §3, the measured x-ray performance reported and discussed in §4, and a relationship between mirror module optical distortion and mechanical distortion is reported and discussed in §5. Finally, §6 summarizes the reported results.

2. THE MIRROR MODULE ASSEMBLIES

Pictured in Figure 1, the *IXPE* satellite observatory consists of three co-aligned grazing incidence x-ray telescopes. The optics are contained within the three mirror module assemblies (MMAs), which are mounted to the Mirror Module Support Structure (MMSS) at the fore end of the observatory. The MMAs, provided by Marshall Space Flight Center (MSFC), each focus x-rays onto one of three corresponding polarization sensitive imaging detector units (DUs), which are mounted on the top deck of the spacecraft bus. A coiled boom will deploy on orbit to separate the MMSS and the spacecraft bus, positioning the optics and detectors at the requisite 4 m focal length distance. The three telescopes are independent and nominally identical; the signal from each telescope will be coadded to produce the final data product.

An *IXPE* MMA, pictured in Figure 2, contains, at its heart, a set of 24 concentrically nested x-ray mirror shells. Each mirror shell has a Wolter 1 prescription with both the parabolic (P) and hyperbolic (H) segments

Further author information: (Send correspondence to S.D.B.)
S.D.B.: E-mail: stephen.d.bongiorno@nasa.gov

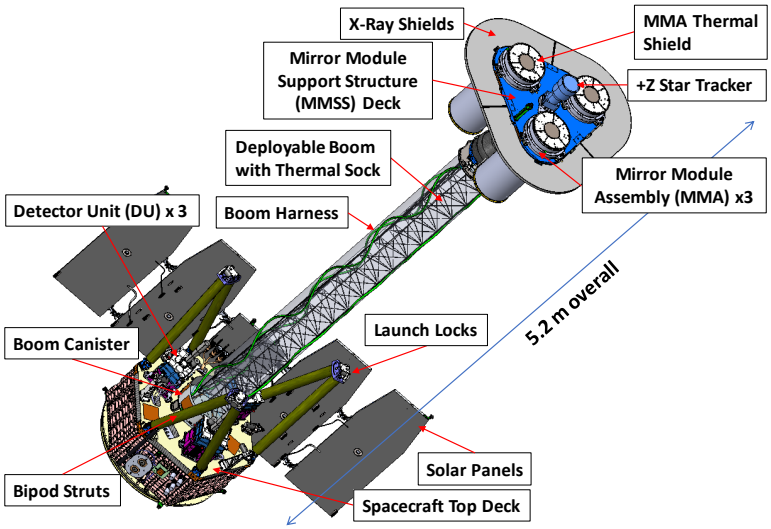

Figure 1. An annotated CAD rendering of the *IXPE* Observatory with the boom and solar panels fully deployed.

electroformed from a single piece of nickel cobalt alloy. The shells were made via an electroforming replication process[6] that begins with diamond turning and lap polishing heavy electroless nickel coated aluminum mandrels to the optical prescription of each shell. A layer of nickel cobalt metal was electroformed onto the mandrel surface and then separated in a cold water bath to produce the shells. Making the P and H segments integral, i.e., from a single piece of metal, greatly simplifies mirror alignment later in the assembly process. The *IXPE* shells are all 600 mm long, range in thickness from 0.179 to 0.254 mm, range in diameter from 165 to 277 mm, and have a focal length of 4 m.

The remainder of the MMA is ancillary hardware to mount the shells, mechanically protect them during integration, dampen their motion during launch vibration, and thermally insulate them in the on-orbit environment. The mirror shells are individually aligned and epoxy bonded at their large end to a stiff support structure called the front spider assembly. Shown in the lower portion of Figure 2, the front spider assembly consists of: the front spider, a 9 spoke structure that is the central mounting point for the different parts of the MMA; the central support tube, a stiff structural member between the front and rear of the MMA; and the front combs, which are the mounting points for the mirror shells. One front comb is epoxy bonded to each front spider spoke and contains 24 slots tangential to the surface of each shell. The comb slot widths are greater than the thickness of the shells so that the large end of the shells can be floated in the slots and bonded in place. Shown in the upper portion of Figure 2, the rear spider attaches the central support tube to the outer housing. It has 18 spokes with one rear comb mounted to each spoke. Similar to the front combs, the rear combs have teeth that fit in the space between the shells without touching, however in the case of the rear, the combs were not epoxy bonded to the shells. Instead, the teeth are covered in a soft polymer to dampen vibration, limit displacement, and prevent the shells from touching one another during launch vibration. The outer structure of each MMA is an aluminum tube called the outer housing which is attached to the rear spider with fasteners and to the front spider with an epoxy bond. Finally, the thermal shields, contributed by Nagoya University, cover the entrance and exit apertures of the MMA. The shields are 1.4 μm thick polyimide films coated with 50 nm of aluminum, mechanically supported by a highly open stainless steel mesh, and mounted to an aluminum frame. The shield film reflects optical and thermal radiation to improve thermal control of the optics, while remaining highly transmissive in the *IXPE* 2-8 keV x-ray bandpass.

3. MMA ASSEMBLY PROCESS

IXPE MMA requirements stated that the optics shall focus 2.3 and 4.5 keV x-rays to a 25 arcsecond half-power diameter (HPD) spot and that the center of the optic must be known to 50 μm (3σ) in the x-y plane (normal to the optical axis). The MMA assembly process was designed such that the optics meet those requirements.

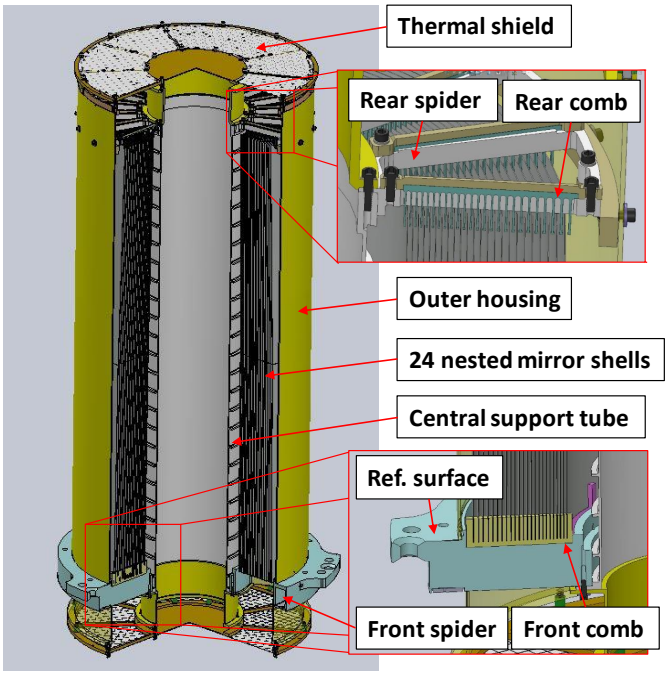

Figure 2. An annotated cut-away CAD rendering of one *IXPE* Mirror Module Assembly. The 24 nested mirror shells are epoxy bonded to the front combs, which are epoxy bonded to the front spider. Thermal shields, which are highly transmissive at x-ray energies, cover the entrance and exit apertures of the optic. The indicated reference surface was measured on the shell alignment station during shell assembly to track shape change of the front spider.

3.1 Mirror Alignment Stations

The shell alignment station aligns, offloads, and stabilizes the mirror shells so that they can be bonded to the front spider assembly with sufficiently precise position, orientation, and shape. Shown in Figure 3, the alignment station consists of a central kinematic mount for aligning the front spider assembly, an upper rig with hanging support wires for positioning and offloading a shell over the front spider assembly, and a spin table for rotating the sensor tower around the shell to measure its position and shape. The *IXPE* shells are thin enough and large enough diameter that they distort unacceptably under self gravity if supported on their bottom edge. To prevent that, the alignment station suspends the shell over the front spider assembly from the top edge via three direct support suspension wires and six offload wires. The direct support wires are actuated by Picomotors in the vertical direction. This enables adjustment of shell tip and tilt. The six adjustable offloaders pull upwards on the shell with $1/9^{\text{th}}$ of its weight to reduce trefoil distortion induced by the three direct support points.

3.2 Mirror Alignment Process

The shell alignment and assembly process began by installing the front spider central support tube assembly on the alignment station via a three-point, spherical washer bolted attachment that is functionally identical to the MMA flight mount on the observatory. This design minimizes bending moments on the spider. Any bending preload placed on the spider at this early stage of assembly will be present when the shells are bonded in place. After shell assembly, unbolting the preloaded MMA from the alignment station will cause the spider to bend back to near original shape and permanently distort the shells. After the front spider was attached to the station, the three Keyence sensors, shown in Figure 3, were used to align the MMA central support tube to the station's rotation axis by adjusting the central kinematic mount. The smallest shell was then transferred from a storage container to the alignment station using the station transfer arm, where it was inspected, attached to the station

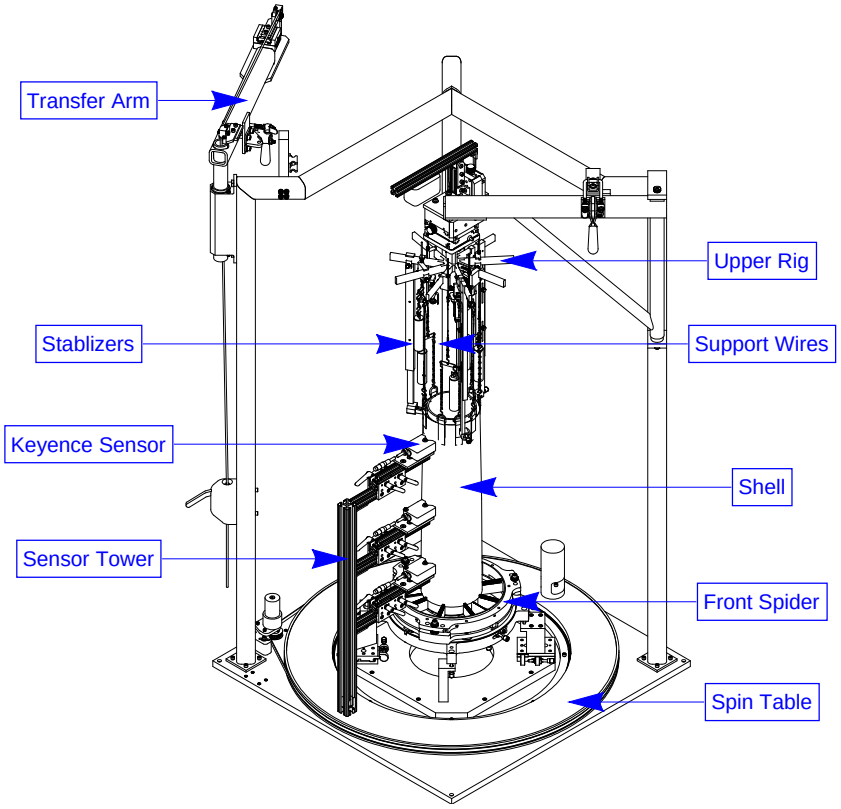

Figure 3. An annotated CAD drawing of the *IXPE* alignment station.

suspension, and the bond areas primed with an adhesion promoter. The shell tilt and position were measured with the alignment station and aligned with Picomotor actuators on the direct support suspension wires and the 3-axis translation stage in the upper rig, respectively.

The shell alignment measurements were made with three Keyence laser displacement sensors positioned near the small end, intersection, and large end of the shell. The sensors rotate around the shell via the alignment station spin table and were sampled at approximately 500 azimuths. This produces displacement waveforms that represents the shell's relative deviation from a circular shape (minus spin table bearing error). Note that while the absolute radius of the shell cannot be determined with this measurement, it is not needed for calculating the relevant shell alignment parameters. The rotation axis of the spin table ball bearing provides the center and tilt reference for all alignment station measurements performed during the shell installation process. In these displacement waveform data, shell centering error appears as an approximately sinusoidal waveform that peaks once per revolution, shell ovality peaks twice per revolution, shell trefoil peaks three times, etc. Fitting a line in three dimensions to the shell centering error in the top, middle, and bottom sensors enables calculation of the shell tilt. Data from two sensors are sufficient to calculate the shell optical axis angle and node position with respect to the station rotation axis. Data from a third sensor was used to calculate deviations in bending of the shell along each azimuth. The root mean square of this waveform is called $\Delta\Delta$R and it is an indicator of low spatial frequency shell performance. If errors are Gaussian-distributed, the $\Delta\Delta$R-predicted half-power diameter (HPD) of the optic point spread function (PSF) will be HPD = 2.698 $\Delta\Delta$R. However, in the case of an *IXPE* shell, structure of the $\Delta\Delta$R waveform is dominated by low order cyclic harmonic functions (oval, trefoil, etc.) and the equivalent HPD is HPD = 4 $\Delta\Delta$R.

A MATLAB application was written to partially automate the iterative aspects of the shell alignment process. First, the application reads and analyzes sensor data and calculates shell center, tilt, and $\Delta\Delta$R performance estimate. The application automatically adjusts the shell position in 5 axes (3-axis translation stage and 2 of 3 Picomotors supporting direct support wires) to align the shell. Finally, the application allows for manual adjustment of stages. Typically between two and five iterations were required to align a shell, depending on initial state, to reach <5 arcseconds tilt and <5 μm centering. Each iteration took approximately three minutes.

After a shell was hung on the alignment station, initial alignment was performed with the shell hanging above front comb slots, in a free-hanging state. A small pendulum motion was observed from room air currents acting on the shell. Mechanical stabilizers were installed to stop the pendulum motion while minimizing any translation of the shell from the bottom of the gravity well. The shell was then realigned, lowered to 0.007 inch above the bottom of the slot and realigned again.

Based on shell shape and optical performance predictions calculated with alignment station data, custom thickness wire shims were inserted between the shell and front comb and the shell was realigned for a final time. If tilt error was less than 25 arcseconds, centering error less than 30 μm, $\Delta\Delta$R less than 20 arcseconds, and the values were stable, the shell was epoxy bonded to the front spider combs. After epoxy cure, the wire shims were trimmed and the bonds photographed on the outside and inside. In this way, shell assembly proceeded from the smallest to the largest shells.

Throughout the shell assembly process, a fourth, downward-facing laser displacement sensor was used to measure the top surface of the front spider and monitor spider bending and tilt drift of the partially assembled MMA. Periodically, the top, radially-oriented Keyence sensor was re-positioned to measure the top of the central support tube and monitor position drift of the partially assembled MMA.

3.3 Bonding

The shell-comb bond design, shown in Figure 4, is a double lap joint where the shell hangs inside the comb slot and epoxy fills the inner and outer gap between the shell and the comb. Each shell-comb bond joint was filled with epoxy by dispensing epoxy drops at the top of the outer comb-shell gap using a syringe fitted with a needle. The epoxy wicked down the outer bond joint, around the large end of the shell, and up the inner bond joint. Loctite EA 9313 Aero epoxy was chosen for this bond because of its low-viscosity, which enables the epoxy to wick into the joint, room temperature cure, which reduces cure-induced mechanical distortions, high strength, low outgassing properties, and flight heritage. In principle, the double-lap bond design is expected to partially balance stress induced by epoxy shrinkage on the inner and outer bond lines and, consequently, reduce shrinkage-induced distortions of the shell shape. We found that for epoxy to wick up to the top of the inner bond gap and produce an adequately wicked joint, larger outer gaps and smaller inner gaps performed better. In this particular bond design, outer bond gaps smaller than 0.005 inch did not consistently reach a fully wicked bond gap on the back side and outer gaps larger than 0.007 inch were not required.

Flattened wire shims, shown in Figure 4 both before and after trimming, were added to the outer bond gap for three reasons: first, to ensure that the outer bond gap was always larger than 0.005 inch and that epoxy wicking would be satisfactory, second, to ensure that the bond gap was within tolerance and would achieve nominal bond strength, and third, to adjust the shell circularity and improve the figure of the shell. On the first point, in a subset of shells, inherent shell ovality prevented achieving the required outer gap on spokes aligned with the major axis of the shell oval. This necessitated use of shims to increase the outer bond gap. On the second point, while adjusting shell circularity with shims did improve shell performance, the benefit was was small. Our ability to optimize shell shape by shimming was limited by the fixed radial locations of the comb groove walls. If optimizing the figure of a shell required a shim less than 0.0055 inch thick, the figure improvement was limited in order to prioritize maintaining acceptable bondline dimensions.

3.4 Operations

IXPE shell assembly took place on four alignment stations in a 10,000 class clean room at MSFC's X-ray and Cryogenic Facility (XRCF). Multiple alignment stations were used to parallelize the shell alignment process in the four modules, which decreased process duration in the overall project schedule. The assembly environment

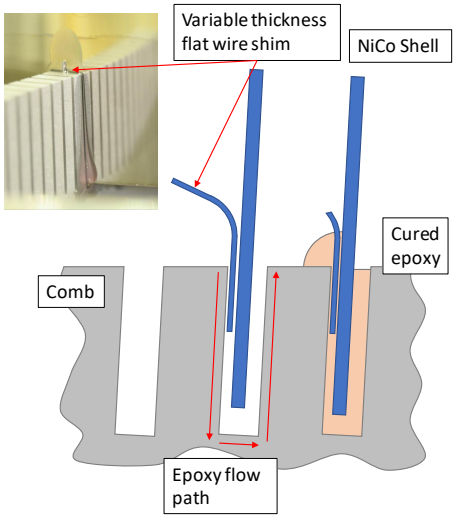

Figure 4. A side-view cut-away illustration of the shell to front spider comb bond design. In this view, the optical axis of the MMA is vertical, off-page to the right of the figure. The shells are seen hanging in the comb slots with wire shims inserted in the outer bond gap. The inner shell (right) is shown with cured epoxy and a trimmed shim. The outer shell (left) is shown with an untrimmed shim inserted, before epoxy has been applied. The photograph shows a shimmed and epoxy-filled shell to front spider comb bond from the outside.

maintained temperature (20±2C) and relative humidity (35-55%) within requirements $> 95\%$ of the time. Bonding operations were paused when the environment was out of range. A typical daily routine during shell assembly lasted for approximately 11 hours, consisting of two overlapping work shifts. In the morning two team members inspected uninstalled shells in their transport containers and prepared shells for installation by applying temporary mounting fixtures used for hanging on the alignment station. Adhesion promoting primer was applied to the shells at approximately noon and allowed to dry for 1 hour, usually over a lunch break. In the afternoon, shells were aligned, shimmed, realigned, and finally epoxy-bonded to the front spider combs at approximately 7 PM. The epoxy was allowed to cure overnight before performing bond inspection, removal of the temporary hanging hardware, and proceeding to the next shell installation the following morning. On many days we were able to install two shells on two different modules. The process was recorded on configuration-controlled procedures with MSFC quality assurance personnel present to witness and verify critical procedure steps such as primer application and final shell alignment.

To reduce schedule duration, shell replication began with the smaller shells and shell assembly began before the entire batch of shells was complete. As a result, the assembly team did not have all shells available to inspect at the beginning of shell assembly and daily shell inspections were able to look about one week ahead. This only resulted in a delay on 2 occasions, once at a shell 9 and once at a shell 12, which were rejected due to edge defects. Both delays were directed onto MMA3, the third MMA in the shell assembly queue. This was done because environmental testing, the next event after MMA assembly, was a serial process and the overall schedule became shorter if the first MMA proceeded to the environmental testing queue as quickly as possible. Successful implementation of this strategy prevented shell assembly delays from delaying the overall project schedule.

4. MMA PERFORMANCE

During shell assembly, shell alignment data were used to track cumulative performance of the MMAs. Metrics of interest were shell centering, tilt, and distortion. Centering error of a single shell displaces the PSF of that shell by the miss-center distance in the overall cumulative PSF. This effect is small since the equivalent angular offset is scaled by the focal length with the typical small-angle plate-scale relation $\delta_{\mathrm{PSF}} \approx \delta_{center}/f$, where δ_{center} is the shell centering error in meters, f is the optic focal length in meters, and δ_{PSF} is the PSF error in radians. In the case of *IXPE*, 20 microns of shell centering error is equivalent to 1 arcsecond of PSF displacement at the

focal plane. Tilt error of a single shell has minimal effect on the PSF because *IXPE*'s monolithic Wolter 1 shells behave like a lens; tilting the shell does not move the focal spot, however it does induce a small amount of coma aberration and reduces throughput. For <30 arcseconds of tilt error, both effects are negligible. Since the shells are constrained by the front spider at their large ends, tilt error correlates with centering error. In contrast to centering and tilt, the shells are very sensitive to certain modes of bending along their long axis. Distortions that cause same-sense angle changes in the P and H segments do not deflect an incident ray, however distortions that cause opposite-sense angle changes in the P and H segments cause significant deflection of an incident ray. For all two-bounce optics, one arcsecond of opposite-sense angle shell distortion will cause four arcseconds of error in a ray traced to the focal plane. In an *IXPE* shell, a modest 5 μm of displacement in the same direction at the large and small ends of the shell causes 13.8 arcseconds of ray deflection at the focal plane.

4.1 Performance Predictions

Shell alignment data were used to predict the HPD of the PSF for each MMA. The results are listed in the fourth row of Table 1. These values do not include HPD contributions from shell shape deviations smaller than approximately the total shell length and do not include scattering effects due to surface roughness. The results are similar for all four MMAs, although MMA 1 and MMA 3 have smaller values than MMA 2 and MMA 4 by 14-19%. All values are in family with the 6-shell engineering model, which had a predicted focal spot width of 13 arcseconds HPD and a x-ray test measured value of 18 arcseconds HPD.

In order to account for additional sources of optical distortion, error in the mandrel shape was also incorporated into the HPD estimate. During the *IXPE* mandrel fabrication process, an interferometer was used to measure the axial figure profiles of the mandrel P and H segments and a coordinate measuring machine (CMM) was used to measure the mandrel circularity, cone angle, P-H intersection location, and radius. Subtracting the optical prescription from the axial figure profile, differentiating by the axial distance variable and calculating the root-mean-square (RMS) yields the mandrel RMS slope error. Assuming Gaussian distributed slope errors, the expected HPD produced by these slope error profiles can be calculated as $\mathrm{HPD} = 1.349\sqrt{(2\sigma_P)^2 + (2\sigma_H)^2}$. The mandrel slope error was then added in quadrature to HPD contributions from the mandrel circularity, cone angle, P-H intersection location, and radius to arrive at a set of 24 mandrel HPD estimates. These values were then combined with an effective-area-weighted average and added in quadrature to the alignment station performance prediction to yield a module HPD prediction that includes all shell and mandrel metrology.

Table 1 lists the predicted MMA HPDs including shell and mandrel metrology (row 5) and shell metrology only (row 4). The simple error propagation method above assumes that these mandrel errors are transferred to the shell during replication and are uncorrelated with the error due to $\Delta\Delta$R and shell centering. All of the predicted HPDs are less than those measured at 2.3 keV, indicating that predicted sources of error are missing.

4.2 Performance Measurements

The four *IXPE* MMAs were individually calibrated at the MSFC Stray Light Test Facility (SLTF) at 2.3, 4.5, and 6.4 keV.[7,8] During test, an x-ray source at a distance of approximately 102 m was shined onto the MMA entrance aperture. The optic focused the incident x-rays onto a CCD detector approximately 4.17 m (finite source focal length) behind the optic. Figure 5 is a composite CCD data image that shows the focused x-ray PSFs and Table 1 lists the measured HPD of the four MMAs at the three calibrated energies.

The measured HPDs of MMA 1 and MMA 4 are closer to their respective shell assembly predicted performance estimates than MMA 2 and MMA 3, indicating that figure degradation may have occurred in these modules after shell assembly. MMA 2 exceeded the MMA-level performance requirement by 4% at 4.5 keV and MMA 3 exceeded the MMA-level performance requirement by 10% at 2.3 keV and 12% at 4.5 keV. Because of availability, MMA 1, MMA 2, and MMA 3 were chosen for flight and integrated into the *IXPE* observatory. The MMA-level HPD requirements on MMA 2 and MMA 3 were waived because the observatory-level HPD performance requirement of 30 arcseconds for all three MMAs was met. Additionally, schedule margin did not allow for substituting MMA 4 for either MMA 2 or MMA 3.

The measured HPDs of MMA 1 and MMA 4 were greater than predictions from as-built shell assembly data. Comparing predicted HPDs to the HPDs measured at 2.3 keV is most relevant because at this energy

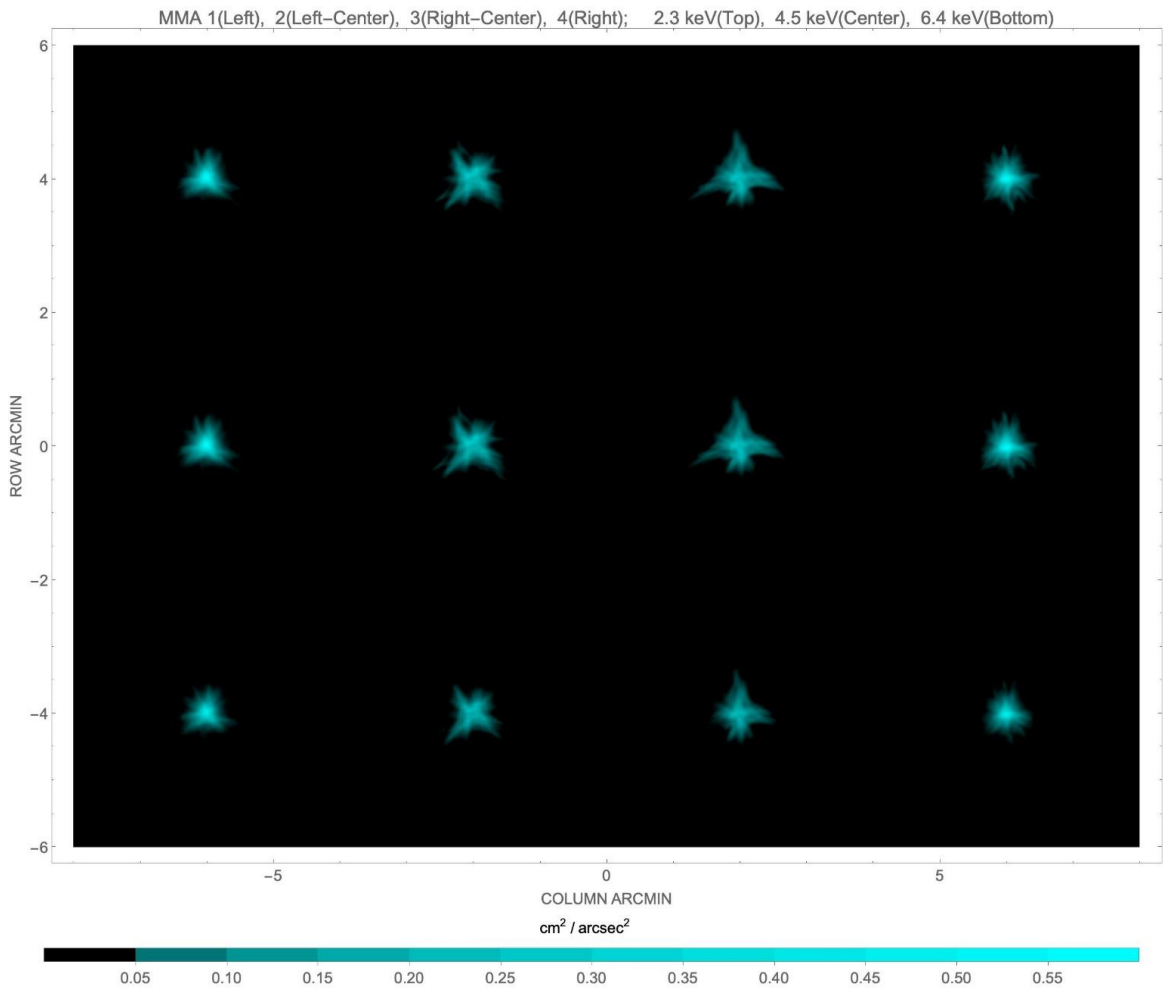

Figure 5. CCD focal spot images taken with the four *IXPE* MMAs at best focus in 2.3, 4.5, and 6.4 keV x-rays.

the inner and outer shells contribute approximately equal flux to the HPD. The metrology based performance predictions may be underestimating the HPD for several reasons. First, for the sake of simplicity, sources of error were added in quadrature, which assumes normally distributed, uncorrelated errors. Second, there may be a systematic uncertainty in the shell $\Delta\Delta$R measurement. Finally, electroformed NiCo shells made by MSFC have greater shape error near the edges than the central portion of the shell. Given that the shell alignment station measures shell shape approximately 5 cm from the shell edge or 20% of the length of one of the segments, the $\Delta\Delta$R-based HPD is likely an underestimate.

To characterize the optical distortions, x-ray images were taken pre- and post-focus. Rays from different azimuths diverge after passing through focus, producing a ring-shaped PSF on a imaging detector. Figure 6 shows CCD image data created by MMA 1, 2, 3 ,and 4 at 57.3, 50.2, 56.6, and 49.4 mm $\pm$ 0.3 mm past focus, respectively. The 18 dark radial lines in each image are shadows of the front and rear spider spokes. In this image, undistorted shells will produce annuli shaped PSFs, however, errors in the optical figure distort the individual shell annuli causing them to blend and become indistinguishable from one another.

The MMA 1 and MMA 4 ring images are azimuthally symmetric, as expected, while MMA2 and MMA3 have significant second harmonic cyclic asymmetry. Ring image azimuths that appear compressed (at a smaller radius in the image) converge behind of focus, and the expanded azimuths converge in front of focus, i.e. astigmatism.

Table 1. Summary of predicted and measured HPD data for the *IXPE* MMAs. Measured values have a standard error of ± 0.3 arcseconds. The "Predicted, shells" HPD was calculated from the area-weighted average of the centering and ΔΔR error measured for each shell during shell assembly. The "Predicted, shells & mandrels" HPD includes the previous value and mandrel HPD. The "Predicted, total" HPD includes the previous two combined with post-assembly astigmatic shell distortion measured with the out of focus x-ray test.

HPD (arcsec.)	MMA 1	MMA 2	MMA 3	MMA 4
Measured, 2.3 keV	19.0	25.0	27.6	20.0
Measured, 4.5 keV	19.9	26.0	28.0	20.8
Measured, 6.4 keV	20.2	25.0	25.8	20.1
Predicted, shells	12.3	14.4	11.6	14.2
Predicted, shells & mandrels	14.1	16.0	13.5	15.8
Predicted, total	15.0	23.5	22.4	17.2

Since these distortions appear in the entire out of focus ring, they are affecting all shells. To quantify the distortion, a second plus third order cyclic harmonic function was fit to the out of focus ring images. Table 2 shows the fit results in the row labeled "Out-of-focus ring".

Table 2. The $n = 2$ cyclic Fourier mode was measured in three data sets: Spider Bend, alignment station measurements of the front spider reference surface (shown in Figure 2) taken before and after unbolting the front spider from the alignment station; Shell 24 ΔΔR, alignment station measurements of shell 24 taken before and after unbolting the front spider from the alignment station; and out of focus ring, out of focus x-ray image data taken during MMA calibration. All data are reported in this table as peak-to-peak values, which can be converted to HPD equivalent by multiplying by 0.7.

MMA bending from unbolting and x-ray astigmatism				
N=2 Fourier pk-pk	MMA 1	MMA 2	MMA 3	MMA 4
Spider bend (μm)	4.0	5.5	1.8	1.6
Shell 24 ΔΔR (arcsec.)	4.4	7.6	0.7	0.9
Out-of-focus ring (arcsec.)	7.0	24.5	25.5	9.5

5. SENSITIVITY TO POST-SHELL-ASSEMBLY SPIDER BENDING

The performance of MMA 2 and MMA 3 was degraded by astigmatic shell distortions larger than those observed in MMA 1, MMA 4, and the engineering model. In the following section we will discuss possible causes of these distortions.

The astigmatic distortion of MMA 2 and MMA 3 likely did not occur during shell installation for two reasons. First, all shells in both MMAs appear to exhibit similar distortion; the astigmatic distortion affected the entire MMA, not a subset of shells. If a characteristic of the shells was the cause, either some shells would not show the effect or all MMAs would show the same effect. Second, both MMA 4 and MMA 2 were constructed on the same alignment station, but MMA 2 shows enhanced distortion while MMA 4 does not. If a characteristic of the alignment station was the cause, these two MMAs would have exhibited similar performance.

Additionally, the astigmatic distortion of MMA 2 and MMA 3 was unlikely to have occurred when the spiders were unbolted from the alignment stations. The difference between alignment station sensor measurements made directly before and after unbolting, shown in Table 2, indicate that unbolting induced small levels of both spider and shell 24 distortion. There is no apparent correlation between increased spider bend or shell 24 astigmatic distortion and the level of astigmatism measured during the out of focus x-ray test, indicating that unbolting did not cause the astigmatic distortion in MMA 2 and MMA 3. Figure 7 shows the unbolting change in shell 24 ΔΔR plotted as a function of unbolting change in spider bending for the four MMAs. A clear correlation is visible, with the slope being an estimate of the *IXPE* MMA optical performance sensitivity to spider bending.

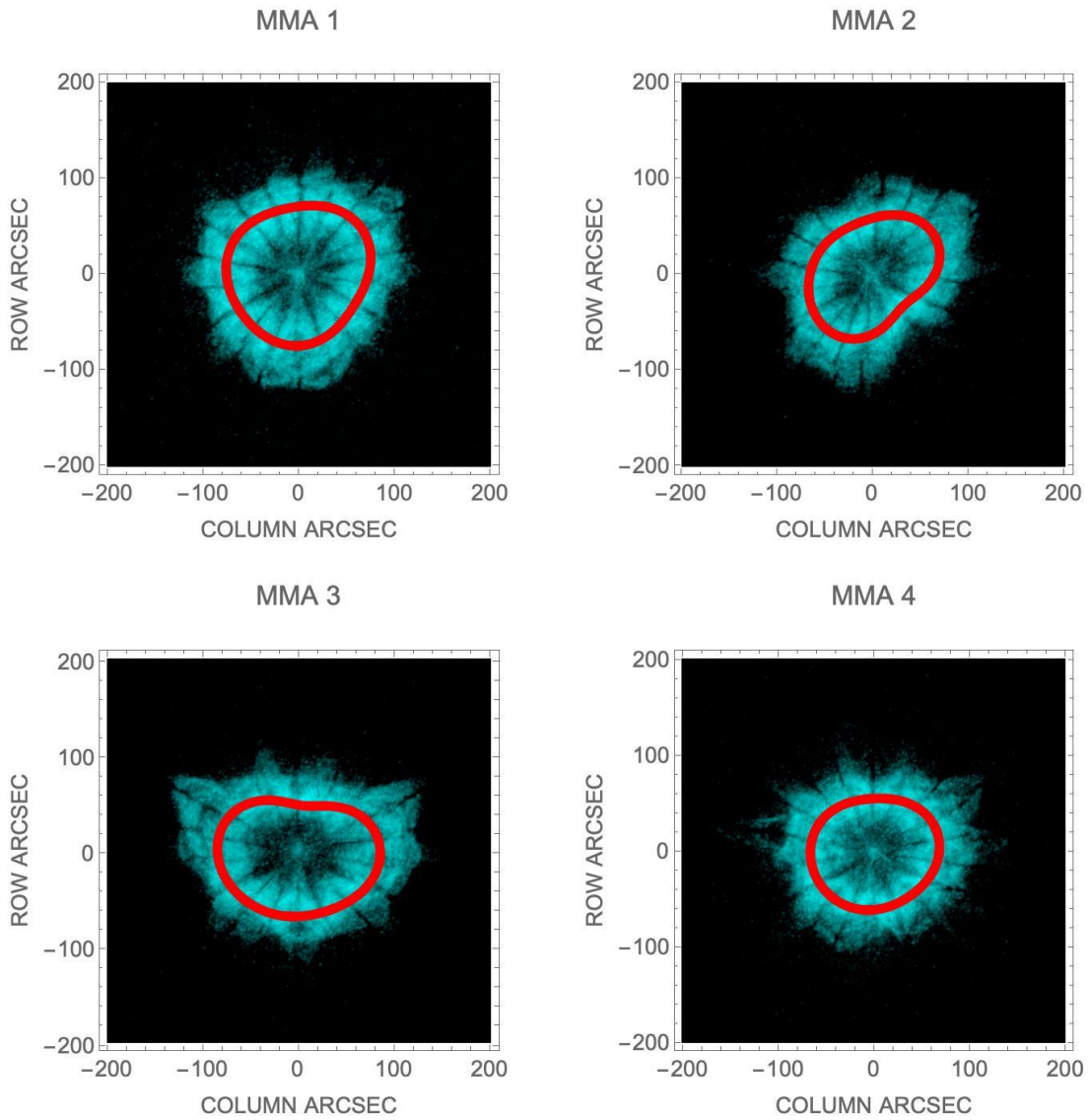

Figure 6. CCD focal spot images taken with the four *IXPE* MMAs using 2.3 keV x-rays and approximately 50 mm out of focus. A second plus third order cyclic harmonic function was fit to the out of focus ring images (red lines).

Therefore, spider bending likely causes astigmatic distortion of the optic, but spider bending during alignment station unbolting did not cause the distortion observed during x-ray test.

Several potential sources of front spider distortion were ruled out during environmental testing and x-ray calibration. MMA 3 was calibrated with and without the thermal shields installed. The amplitude of the distortion changed < 2 arcseconds, ruling out misalignment between the thermal shields and the thermal shield mounting flange as the source of the astigmatic distortion. Also, after initial calibration, MMA 3 was rotated by 120 degrees in the calibration fixture and partially recalibrated. In the recalibration data, the magnitude of distortion changed < 2 arcseconds and the orientation rotated 120 degrees in the same direction that the MMA was rotated, ruling out gravity sag and the bolted interface between the MMA and the calibration fixture as sources of the distortion. MMA 2 was calibrated before and after proto-flight vibration environmental testing.

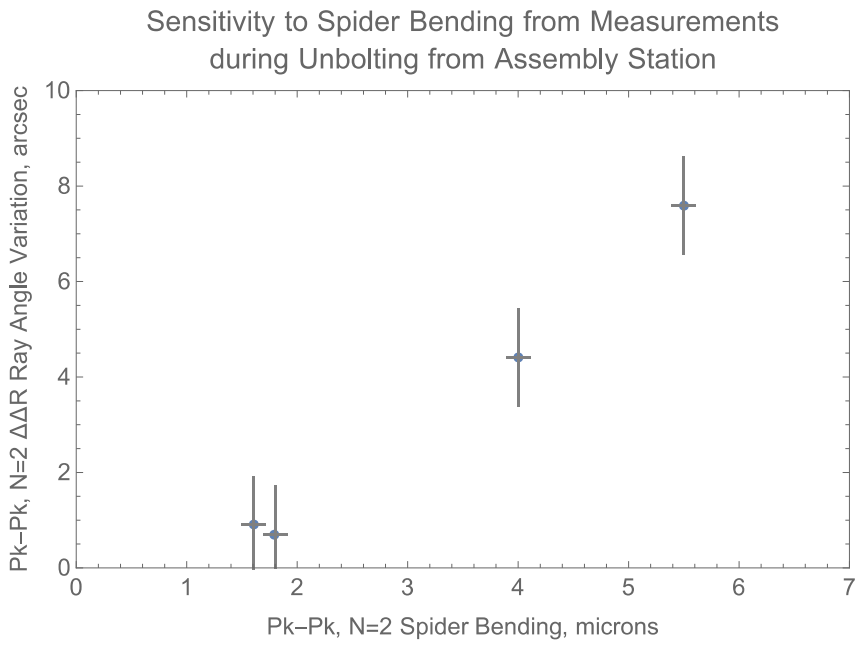

Figure 7. Measured astigmatism in the x-ray out of focus image plotted as a function of change in spider bending measured at the front spider reference surface plotted as a function of for the four *IXPE* MMAs.

This module exhibited similar enhanced astigmatic distortion before and after test, ruling out vibration as a source of the distortion.

The astigmatic distortion of MMA 2 and MMA 3 may have occurred during an MMA assembly process after the MMAs were removed from the alignment stations. Possible sources of the distortion:

- shape error in the temporary front handling fixture distorted the front spider and this distortion became permanent when the outer housing was bonded to the front spider,
- the front spider distorted under gravity load of the outer housing during outer housing bonding,
- the outer housing and central support tube were stressed when the rear spider was bolted in place,
- shape error in the rear handling fixture distorted the front spider and was made permanent when the front outer thermal shield support was bonded to the front spider.

In all suggested scenarios, a component stressed the front spider, that stress distorted all of the shells, and that distortion was made permanent by a subsequent step in MMA assembly (bolted interface or epoxy bond). A full fault tree analysis to find the root cause of the distortion has not yet been performed because the MMAs met requirements. However, for the benefit of future programs, we intend to run this issue to ground.

To produce a more complete accounting of optical distortion in the MMAs, the astigmatic error measured in the out of focus ring images was added to the shell assembly and mandrel errors listed in Table 1. Given that astigmatic distortion at the end of shell assembly was relatively small, this additional error term accounts for astigmatic distortion added after shell assembly with minimal double counting.

Lessons learned from this investigation include:

- sufficient mechanical stiffness in the front spider is important for reducing assembly-related optical distortion;

- during mirror module mechanical design, all components that contact the spider should be examined for potential to induce distortion;
- during mirror module assembly process design, all assembly steps after shell installation should be examined for potential to induce shell distortion;
- the front spider should be attached to fixtures in such a way that distortion during critical operations is kept below acceptable values and this should be verified with measurements.

6. SUMMARY

Assembly of the three flight and one spare *IXPE* mirror module assemblies took place with a crew of five people at MSFC from October 2019 to July 2020, with a four month pause during the COVID-19 shutdown from March to May 2020. The measured x-ray performance of two mirror modules (MMA 1 and MMA 4) was in approximate agreement with predictions from the build data. The measured x-ray performance of the remaining two modules (MMA 2 and MMA 3) did not agree with build data predictions and indicated the presence of additional optical distortion. Due to project schedule constraints and relative module delivery times, MMA 1, MMA2, and MMA3 were chosen as flight modules and integrated into the *IXPE* spacecraft, even though MMA 4 had better optical performance. MMA 2 and MMA 3 did not fully meet the *IXPE* MMA-level optic PSF HPD requirement of 25 arcseconds, however the three combined flight mirror modules and detectors met the observatory-level performance requirement of 30 arcseconds.

IXPE is currently expected to launch from Kennedy Space Center on a Falcon-9 rocket no earlier than December 13, 2021.

REFERENCES

[1] O'Dell, S. L., Baldini, L., Bellazzini, R., et al., "The Imaging X-ray Polarimetry Explorer (IXPE): technical overview," in [*Space Telescopes and Instrumentation 2018: Ultraviolet to Gamma Ray*], den Herder, J.-W. A., Nikzad, S., and Nakazawa, K., eds., **10699**, 468 – 481, International Society for Optics and Photonics, SPIE (2018).

[2] O'Dell, S. L., Attinà, P., Baldini, L., et al., "The Imaging X-Ray Polarimetry Explorer (IXPE): technical overview II," in [*UV, X-Ray, and Gamma-Ray Space Instrumentation for Astronomy XXI*], Siegmund, O. H., ed., **11118**, 248 – 261, International Society for Optics and Photonics, SPIE (2019).

[3] Soffitta, P., Attinà, P., Baldini, L., et al., "The Imaging X-ray Polarimetry Explorer (IXPE): technical overview III," in [*Space Telescopes and Instrumentation 2020: Ultraviolet to Gamma Ray*], den Herder, J.-W. A., Nikzad, S., and Nakazawa, K., eds., **11444**, 1017 – 1028, International Society for Optics and Photonics, SPIE (2020).

[4] Ramsey, B. D., Attina, P., Baldini, L., et al., "The Imaging X-Ray Polarimetry Explorer (IXPE): technical overview IV," in [*UV, X-Ray, and Gamma-Ray Space Instrumentation for Astronomy XXII*], Siegmund, O. H., ed., **11821**, 225 – 236, International Society for Optics and Photonics, SPIE (2021).

[5] Soffitta, P., "IXPE the Imaging X-ray Polarimetry Explorer," in [*UV, X-Ray, and Gamma-Ray Space Instrumentation for Astronomy XX*], Siegmund, O. H., ed., **10397**, 127 – 135, International Society for Optics and Photonics, SPIE (2017).

[6] O'Dell, S. L., Atkins, C., Broadway, D. M., et al., "X-ray optics at NASA Marshall Space Flight Center," in [*EUV and X-ray Optics: Synergy between Laboratory and Space IV*], Hudec, R. and Pina, L., eds., **9510**, 7 – 20, International Society for Optics and Photonics, SPIE (2015).

[7] Thomas, N. E., Baumgartner, W., Champey, P. R., et al., "The Marshall 100-meter x-ray beamline," in [*Optics for EUV, X-Ray, and Gamma-Ray Astronomy X*], O'Dell, S. L., Gaskin, J. A., and Pareschi, G., eds., **11822**, International Society for Optics and Photonics, SPIE (2021).

[8] Baumgartner, W. H., Ramsey, B., Thomas, N., et al., "Ground Calibration of the IXPE Optics and Telescope," in [*UV, X-Ray, and Gamma-Ray Space Instrumentation for Astronomy XXII*], Siegmund, O. H., ed., **11821**, International Society for Optics and Photonics, SPIE (2021).